Article

Many-body Hilbert space scarring on a superconducting processor

Pengfei Zhang [1,7], Hang Dong[1,7], Yu Gao[1,7], Liangtian Zhao[2], Jie Hao[2], Jean-Yves Desaules [3], Qiujiang Guo [1,4], Jiachen Chen[1], Jinfeng Deng[1], Bobo Liu[1], Wenhui Ren[1], Yunyan Yao[1], Xu Zhang [1], Shibo Xu[1], Ke Wang[1], Feitong Jin[1], Xuhao Zhu[1], Bing Zhang[4], Hekang Li [1,4], Chao Song[1,4], Zhen Wang [1,4], Fangli Liu [5], Zlatko Papić [3], Lei Ying [1,4] ✉, H. Wang [1,4] ✉ and Ying-Cheng Lai [6] ✉
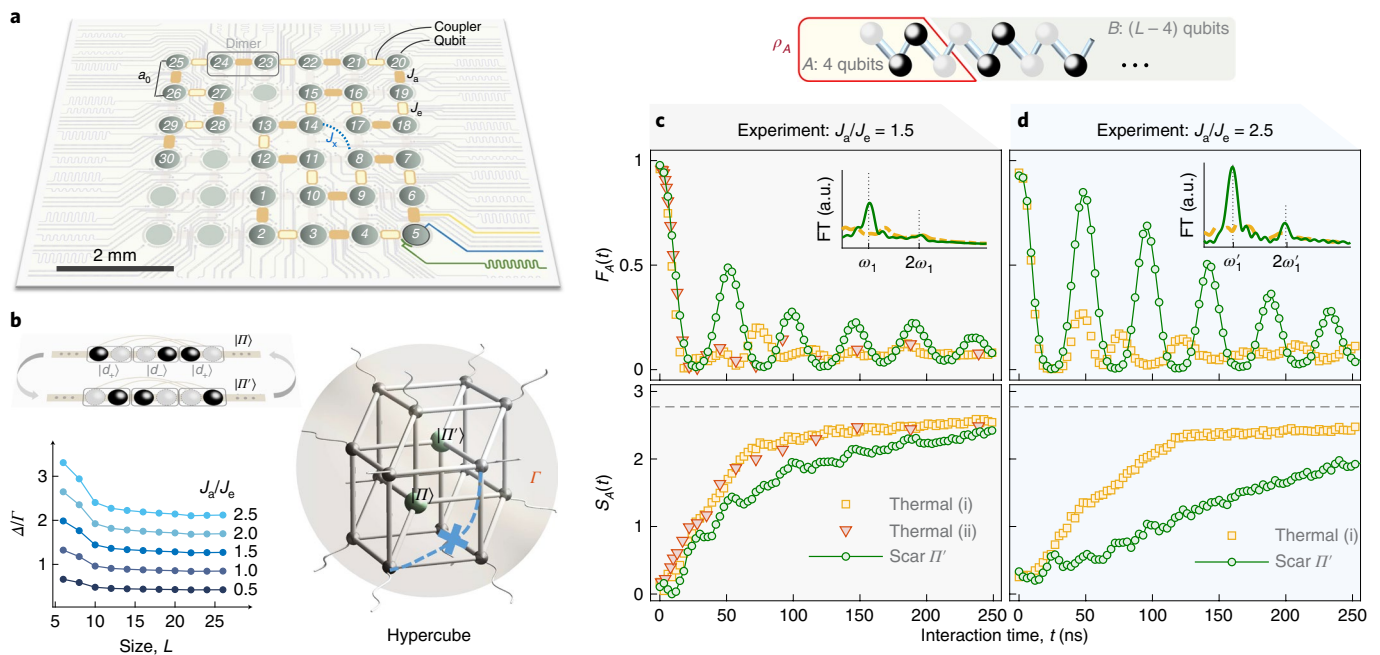
Quantum many-body scarring (QMBS) is a recently discovered form of weak ergodicity breaking in strongly interacting quantum systems, which presents opportunities for mitigating thermalization-induced decoherence in quantum information processing applications. However, the existing experimental realizations of QMBS are based on systems with specific kinetic constrains. Here we experimentally realize a distinct kind of QMBS by approximately decoupling a part of the many-body Hilbert space in the computational basis. Utilizing a programmable superconducting processor with 30 qubits and tunable couplings, we realize Hilbert space scarring in a non-constrained model in different geometries, including a linear chain and quasi-one-dimensional comb geometry. By reconstructing the full quantum state through quantum state tomography on four-qubit subsystems, we provide strong evidence for QMBS states by measuring qubit population dynamics, quantum fidelity and entanglement entropy after a quench from initial unentangled states. Our experimental findings broaden the realm of scarring mechanisms and identify correlations in QMBS states for quantum technology applications.

Strongly coupled quantum systems provide a wealth of opportunities for fundamental physics as well as practical applications that utilize quantum entanglement[1–4]. However, the majority of such systems, even if they are perfectly isolated from the external world, undergo chaotic dynamics and information scrambling[3,5–8]—the process described by the so-called eigenstate thermalization hypothesis (ETH)[9–12]. Developing methods to defy the ETH so as to preserve quantum information in long-lived dynamic states has become an important goal of quantum sciences[13].

The recent discovery of quantum many-body scarring (QMBS)[14,15]—a many-body analogue of the scarring phenomena in quantum billiards[16]—has shown that certain many-body systems can host non-thermalizing eigenstates at high-energy densities above their ground state. In such systems, some special initial states have long-lived coherent dynamics, in stark contrast to the rapid thermalization from other initial conditions. This offers a new route for designing non-ergodic dynamics compared with, for example, fine-tuning the couplings of systems to make them integrable, and it avoids the need

Fig. 1 | Experimental setup and identification of QMBS states via quantum state tomography. a, Experimental SC circuit of device I with qubits and couplers in a square geometry. The light-grey dashed rectangles represent dimers that constitute the chain with intracoupling J_a, intercoupling J_e and small cross-coupling J_x. **b**, Schematic (upper left) of the dynamics of the collective dimer states $|\Pi\rangle$ and $|\Pi'\rangle$. Numerics of the ratio Δ/Γ as a function of system size L for different ratios of J_a/J_e, with $J_x/2\pi$ in the range of [0.3, 1.2] MHz (lower left). Four-dimensional hypercube in the Hilbert space (right). **c**, Quantum state tomography for the four-qubit fidelity $F_A(t)$ and entanglement entropy $S_A(t)$ in a

30-qubit chain for thermalizing initial states, namely, $|0101...0110\rangle$ (i) and $|01001...100110110\rangle$ (ii), and the QMBS state Π' (green). The couplings are $J_a/2\pi = 1.5J_e/2\pi \simeq -9$ MHz. The inset shows the Fourier transform of the four-qubit fidelity with the peak at $\omega_1/2\pi \approx 21$ MHz. The dashed grey line in the bottom panel represents the maximal thermal entropy for the subsystem, approaching to $4\ln(2)$. **d**, Same data as **c**, but for different couplings, namely, $J_a/2\pi = 2.5J_e/2\pi \simeq -10$ MHz from device II and $\omega_1'/2\pi \approx 22$ MHz. Schematics in **c** and **d** illustrate the bipartition of the system.

to strongly disorder the system to drive it into a many-body localized phase[17–20]. Because of their ability to suppress thermalization for only those selected states, QMBS is expected to be useful for storing quantum information[14], generating Greenberger–Horne–Zeilinger entangled state[21] and in quantum-enhanced sensing[22]. However, although there has been a proliferation of theoretical studies on QMBS[23–34], the experimental realizations of QMBS remain in short supply. The existing QMBS experiments remain focused on the kinetically constrained PXP model[35,36], which has been effectively realized using Rydberg atoms[13,37] and ultracold bosons in optical lattices[38]. More recently, ultracold lithium-7 atoms in an optical lattice, which realize the Heisenberg spin model, have been explored as a host of non-thermalizing helix states, reminiscent of QMBS[39].

In this Article, we report the observation of a new class of QMBS states on a superconducting (SC) processor. In contrast to previous realizations in kinetically constrained Rydberg atom arrays, we design QMBS by weakly decoupling one part of the Hilbert space in the computational basis. Our approach is inspired by the topological structure of the Su–Schrieffer–Heeger (SSH) model of polyacetylene[40], which we utilize to create a nearly decoupled subspace with the structure of the hypercube graph. This subspace gives rise to emergent QMBS phenomena, including many-body revivals from special initial states residing in the hypercube, as well as the band of scarred eigenstates. Meanwhile, the entire system thermalizes due to weak cross-couplings between non-nearest-neighbouring qubits. One of the advantages of our SC platform is the tunable XY coupling between qubits (Methods) on a 6 × 6 square lattice configuration, which enables us to emulate many-body systems with both one-dimensional (1D) and quasi-1D systems with a comb shape. We investigate circuits of up to 30 qubits and 29 couplers, with the Hilbert space dimension of 155,117,520—far

beyond the limits of classical simulation. The measurements of population dynamics and quantum state tomography for entanglement entropy and quantum fidelity provide strong evidence of the emergence of robust QMBS states, as we demonstrate by directly comparing their slow dynamics against conventional thermalizing states. Our realization of a new QMBS paradigm in a solid-state SC platform enables a systematic exploration of the fundamental physics of many-body scarring in systems with highly tunable interactions and configurable lattice topology beyond one spatial dimension.

Mechanism of Hilbert space scarring

Our experiment utilizes a two-dimensional SC qubit array[4,41] (Fig. 1a), which features high-density integration and high degree of controllability over local couplings[42,43], allowing to emulate different models in a single device. We first consider the 'snake'-like qubit layout (Fig. 1a). This layout exploits the structure of the SSH chain[40], where the intra-dimer coupling $J_{i,i+1} = J_a$ ($i \in$ odd) is slightly stronger than the inter-dimer coupling $J_{i,i+1} = J_e$ ($i \in$ even). This model is motivated as follows. In the limit $J_a \gg J_e$, each dimer with one photon behaves as a nearly free two-level system. Hence, the SC qubit system is isomorphic to a free spin-1/2 paramagnet. Such a system supports quantum revivals, but they are essentially of the single-particle origin. When J_a and J_e are comparable in magnitude, they are in the regime of the SSH model where quench dynamics from fully polarized and Néel initial states has recently been investigated[44,45]. Although the Néel state does not display persistent revivals, we will show below that it is possible to identify, based on the graph structure of the Hamiltonian, other initial states that do exhibit quantum revivals, even after the interactions break integrability and cause the system to thermalize for most of the other initial states.
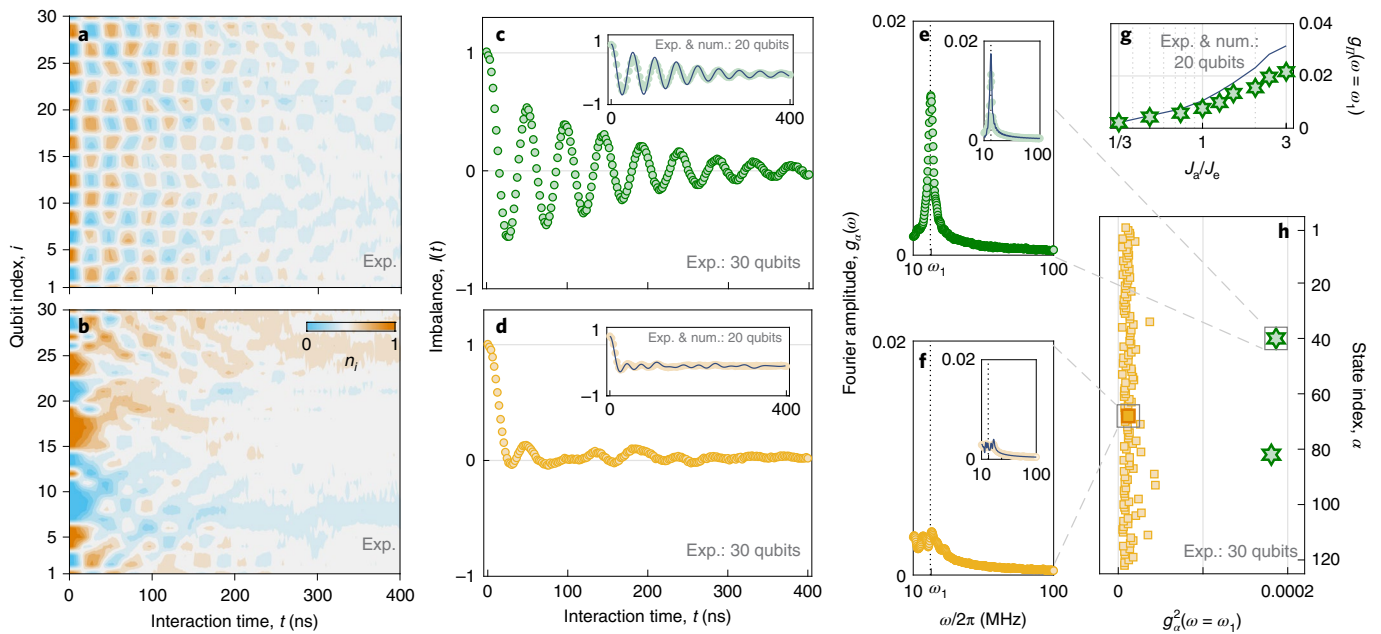
Fig. 2 | Experimentally observed qubit dynamics. a,b, Contour diagrams (device I) of the experimental (Exp.) qubit population as a function of interaction time for a QMBS state (**a**) and a rapid thermalizing state (**b**). **c,d,** Generalized imbalance $I(t)$ extracted from the plots in **a** (**c**) and **b** (**d**) as a function of interaction time. The insets show the imbalance dynamics from experiments (dots or circles) and numerical (num.) simulations (solid curves) in a 20-qubit chain. **e,f,** Fourier transformation amplitude of the imbalance in **c** (**e**) and **d** (**f**), which characterizes the squared overlap between the initial states and energy

eigenstates. The time window for the fast Fourier transform is extended to 4 μs with zero padding. **g,** Fourier peak as a function of coupling ratio J_a/J_e in a chain of $L = 20$ from experimental measurements (green hexagrams) and numerical simulations (solid curve). **h,** Squared Fourier amplitude $g_\alpha^2(\omega = \omega_1)$ of $|\alpha\rangle$ for 120 randomly chosen initial product states, including two QMBS states (green hexagrams) that clearly stand out from the rest of the thermalizing product states (yellow squares). The simulation parameter values in **c–f** are $J_a/2\pi = -9.3$ MHz, $J_e/2\pi = -6.1$ MHz and $J_x/2\pi \in [0.3, 1.2]$ MHz.

We identify candidate QMBS states based on their special location in the Hamiltonian adjacency graph. Each dimer has four states: $|d_0\rangle = |00\rangle$, $|d_1\rangle = |11\rangle$, $|d_+\rangle = |10\rangle$ and $|d_-\rangle = |01\rangle$. At half-filling, that is, with the number of photons N equal to half the total number of qubits L, a special class of dimerized states can be identified. All these states have one photon in each dimer (that is, they only contain d_+ or d_-); they form the vertices of an N-dimensional hypercube, with all the edges (that is, Hamiltonian matrix elements) of equal weight (Fig. 1b). Among these, the collective states $|\Pi\rangle = |d_+d_-d_+d_-\cdots\rangle$ and $|\Pi'\rangle = |d_-d_+d_-d_+\cdots\rangle$ have the unique property of only having intradimer couplings and they are located at opposite corners of the hypercube (Fig. 1b). This suppresses the leakage of information in the states $|\Pi\rangle$ and $|\Pi'\rangle$, with the other states in the hypercube playing the role of a 'buffer' area. To show that $|\Pi\rangle$ and $|\Pi'\rangle$ are bona fide QMBS, it is crucial to demonstrate that (1) revivals from $|\Pi\rangle$ and $|\Pi'\rangle$ states persist when we break integrability and allow all the states to thermalize; (2) the revivals are a 'many-body' effect, that is, they are not due to the hypercube being trivially decoupled from the rest of the Hilbert space.

In our setup, thermalization is naturally induced by irregular cross-couplings, $J_x/2\pi$, experimentally in the range of $[0.3, 1.2]$ MHz—the couplings between two next-nearest-neighbour qubits with a physical separation distance of $a_{ij} = \sqrt{2}a_0$, where $a_0 \approx 0.8$ mm is the separation distance of two nearest-neighbour qubits. These random couplings break the reflection symmetries of the circuit and thermalize the system, as confirmed by the energy-level spacings following the Wigner–Dyson distribution with the parameter $\langle r \rangle \approx 0.53$ (Supplementary Information). We note, however, that it is also possible to break integrability via translation-invariant perturbations that even enhance the revivals from the $|\Pi\rangle$ and $|\Pi'\rangle$ states, further demonstrating the importance of many-body effects (Supplementary Information).

To quantify the impact of the hypercube on the dynamics, note that the sum of the hypercubic-thermal couplings (interdimer couplings

and cross-couplings) gives the decay rate Γ of the hypercube to the thermalized parts. The summation of intra-hypercubic couplings Δ is given by the number of hypercubic edges, that is, $\Delta = N \times 2^{N-1}J_a$. Their ratio Δ/Γ converges to a finite value for different values of J_a/J_e (Fig. 1b), which shows that the hypercube is not trivially disconnected from the rest of the Hilbert space. At the same time, although other parts of the Hilbert space are frustrated by irregular J_x couplings, no two states within the hypercube are linked by them; therefore, the hypercubic structure is robust since the cross-couplings do not affect the dynamics within it.

Tomographic measurements

The experimental observations of QMBS states in our SC processor are presented in Fig. 1c,d. With high-precision control and readouts, we were able to perform tomography measurements to directly obtain elements of the reduced density matrix $\boldsymbol{\rho}_A$ of subsystem A. From these, we evaluate the dynamics of the subsystem fidelity as $F_A(t) = \text{Tr}[\boldsymbol{\rho}_A(0)\boldsymbol{\rho}_A(t)]$ and bipartite entanglement entropy as $S_A(t) = \text{Tr}[\boldsymbol{\rho}_A(t)\log[\boldsymbol{\rho}_A(t)]]$. The complexity of such measurements rapidly grows with the size of subsystem A; below, we consider A to be four qubits (schematic above Fig. 1c). We emphasize that although we consider a relatively small subsystem here, the four-qubit fidelity F_A mirrors the behaviour of the full fidelity, as numerically shown in the Supplementary Information. The data points in Fig. 1c give, for a 30-qubit chain, the time evolution of the four-qubit fidelity for the collective state $|\Pi'\rangle$ and two typical thermalizing states. The fidelity of the QMBS state exhibits revivals with a period of about 50 ns and the peak value of the first revival can be as high as 0.5, whereas no such revivals occur for the thermalizing states.

In Fig. 1c (bottom), we measure the time evolution of $S_A(t)$ for QMBS and two conventional thermalizing states. Compared with the thermalizing states, the scarred dynamics leads to a slightly slower growth of entanglement entropy, superposed with oscillations whose frequency is twice that of fidelity revivals (Fig. 1c). This double frequency is due

to the fact that the system oscillates between $|\Pi\rangle$ or $|\Pi'\rangle$ states. Thus, entropy is locally minimized or maximized (depending on the choice of subsystem) when the system is near either of these states, whereas the fidelity only measures the return to the initial state $|\Pi'\rangle$. In our experiment, both scarred and thermalizing states ultimately approach the Page entropy, that is, 4ln(2), of the four-qubit subsystem.

We note that scarring, particularly the rate of entanglement entropy growth, can be improved by increasing the coupling ratio J_a/J_e to 2.5 (Fig. 1d). This ratio controls the coupling of the hypercube to the rest of the Hilbert space, as we emphasized above. Furthermore, as shown in the Supplementary Information, some regular perturbations, for example, a next-next-nearest-neighbour coupling, can efficiently suppress the entropy growth of the scarred state. Similarly, the periodic driving of a local potential can noticeably enhance the scarred fidelity revivals and inhibit the entropy growth, as also observed in Rydberg atoms[13].

Qubit dynamics beyond the limit of classical simulations

The measurement of the qubit population dynamics is more time saving than tomography; therefore, it allows us to further probe thermalization by randomly choosing many initial product states. The generalized population imbalance is defined as $I(t) = (1/L)\sum_i^L \langle S_i^z(0)\rangle\langle S_i^z(t)\rangle$. The imbalance is determined by the overlaps $|\langle E_n|\alpha\rangle|^2$ of energy eigenstates $|E_n\rangle$ with initial state $|\alpha\rangle$ and phase factors $\exp(-i(E_n - E_m)t/\hbar)$, where m and n are eigenstate indices and $\hbar$ is the reduced Planck constant. For a thermalizing initial state, the phases are essentially random and the initial state has roughly equal support on all the energy eigenstates. Thus, any imbalance rapidly diffuses to a value exponentially small in the system size and it cannot be detected via local operators at late times. By contrast, a QMBS initial state has appreciable overlap only on a few eigenstates with phases set to integer multiples of a single frequency. This allows a QMBS state to display a persistent quantum revival even at relatively late times.

The evolution of population imbalance in a 30-qubit chain is shown in Fig. 2a,b, which contrasts a QMBS state against a typical thermalizing state. The QMBS state exhibits remarkable oscillations that are absent in the thermalizing state. The imbalance $I(t)$ is plotted in Fig. 2c,d, which distinctly reveals the differences between the two initial states. In general, for the thermalizing state, after about 30 ns, the imbalance has nearly fully decayed to about half a photon in each qubit.

The distinct features of QMBS states can be further highlighted through the overlap between the product states and eigenstates $|\langle\alpha|E_n\rangle|^2$, which can be represented by the Fourier spectrum of the imbalance for the QMBS (Fig. 2e) and thermalizing (Fig. 2f) states. The peak value of the Fourier spectrum $g_\alpha(\omega)$ with the first-order domain eigenstates is $\omega_1/2\pi \approx 21$ MHz. We test 120 random initial product states and find that the $g_\alpha^2(\omega = \omega_1)$ values of the QMBS states are unambiguously distinct from those of conventional thermalizing states (Fig. 2h). Note that, for the cases shown in Fig. 2a–f, carrying out the exact simulations is computationally impractical. Instead, the experimental data have been validated by a numerical simulation on a smaller system with $L = 20$ (Fig. 2c–f, insets), demonstrating excellent agreement.

The advantage of our experimental system—the tunable effective couplings between two nearest-neighbour qubits—allows us to systematically probe the stability of QMBS states as the ratio of the intra- and interdimer couplings (J_a/J_e) is varied. As shown in Fig. 2g, the numerical and experimental results indicate that QMBS states consistently emerge in the regime of $J_a/J_e \gtrsim 1$. Moreover, even for a chain with uniform nearest-neighbouring couplings $(J_a/J_e = 1)$, the value of $g_\Pi(\omega_1) \approx 0.0080$ is sufficiently large compared with the average value of the thermal states, which is around 0.0035 (Fig. 2h). This implies that scarring is not trivially induced by the imbalance between intra- and interdimer couplings since this value difference of ~0.0045 is above the measurement standard deviations given in the Supplementary Information. In the regime of large coupling $(J_{a,e}/2\pi > 12$ MHz), the effective
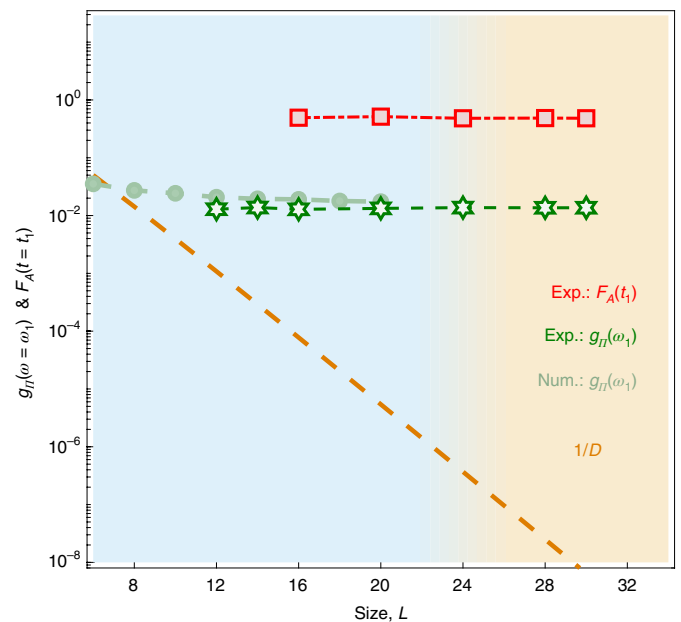

Fig. 3 | Scaling behaviour. Scaling of the first revival peak $F_A(t_1 \approx 52$ ns) of subsystem A, Fourier amplitude $g_\Pi(\omega_1)$ and inverse Hilbert space dimension $1/D$ versus the system size for $J_a/2\pi \simeq -9$ MHz and $J_e/2\pi \simeq -6$ MHz. The light-blue area denotes the regime where classical simulations using the exact diagonalization method are feasible.

Hamiltonian describing our system (equation (3)) is no longer accurate due to the population leakage to couplers. Due to the fast growth of the Hilbert space dimension, we did not explore this coupling regime.

To verify the persistence of the QMBS states for different system sizes, we perform measurements on chains of sizes of $L = 12–30$. The time evolution of imbalance, four-qubit fidelity and entanglement entropy were found to behave consistently for different system sizes, confirming the robustness of scarring in the collective states $|\Pi\rangle$ and $|\Pi'\rangle$. The relatively small variations between the imbalance and entanglement entropy for different system sizes are due to the difference in the cross-couplings and couplers. The Fourier amplitude $g_\Pi(\omega_1)$ and fidelity $F_A(t_1)$ at the first revival exhibit a plateau for $L > 16$ (Fig. 3), whereas for a random initial state, these quantities are expected to exponentially decrease with system size. The plateau in scaling suggests that the QMBS states persist in the regime of large system sizes approaching the thermodynamic limit.

Many-body scars on a comb

Our programmable SC circuit allows us to emulate more complex topology beyond one dimension. We have experimentally studied the QMBS states in a comb geometry (Fig. 4a), which consists of a 1D 'backbone' decorated with linear 'offshoots'. Previous studies of quantum comb systems with offshoots of random lengths were shown to exhibit localization, including 'compact' localized states for which the localization length can vanish along the backbone[29,46]. In our realization, we take the offshoots to be of the same length, and we fix $L = 2N = 20$. We consider each offshoot to be a dimer; similar to the 1D chain, we set the interdimer couplings to $J_e/2\pi \simeq -6$ MHz and intradimer couplings to $J_a/2\pi \simeq -9$ MHz. In contrast to the chain geometry, the QMBS states in the comb geometry are $|\Theta\rangle = |d_+d_+\cdots\rangle$ and $|\Theta'\rangle = |d_-d_-\cdots\rangle$. These states are also characteristically distinct from the conventional thermalizing states, as revealed by the squared Fourier amplitude (Fig. 4b). The striking contrast between a QMBS state and thermalizing state can be seen at a more detailed level (Fig. 4c–e), which shows the time evolution of imbalance $I(t)$, four-qubit fidelity, and entanglement entropy for the $|\Theta'\rangle$ state and a typical thermalizing state.
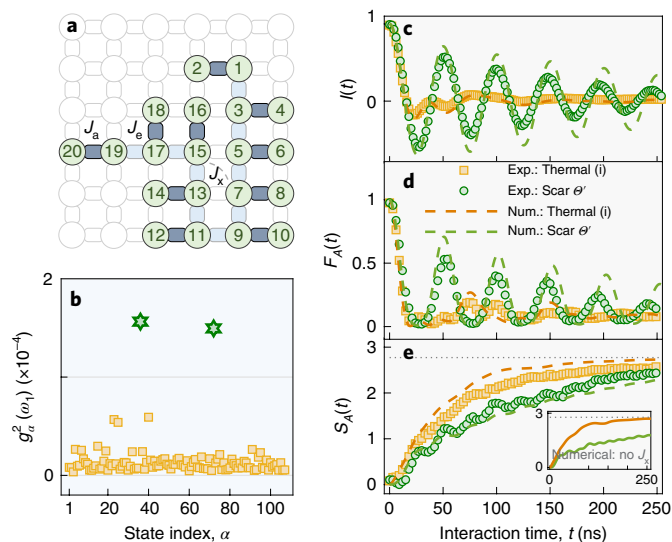
Fig. 4 | QMBS states in a comb tensor system. a, Comb tensor topology on the SC processor (device I) with $L = 20$ qubits. **b**, Squared Fourier amplitude $g_\alpha^2(\omega = \omega_1)$ for randomly chosen initial product states. The QMBS states (green hexagrams) are characteristically distinct from the conventional thermalizing product states. **c**–**e**, Dynamics of the imbalance, four-qubit fidelity and four-qubit entanglement entropy for the $|\Theta'\rangle$ state (green circles) and a randomly chosen product state $|00111000111010011001\rangle$ (yellow squares (i)) for a 20-qubit comb. The dashed curves denote the numerical results. The inset in **e** shows the numerical result in the case without cross-couplings J_x, where the scarred state shows a much slower entropy growth from the thermalizing state. The couplings are tuned to $J_a/2\pi \simeq -9$ MHz and $J_e/2\pi \simeq -6$ MHz.

Our experimental results show that the scarring signatures are the most striking at intermediate times, whereas at very late times, the system relaxes to a thermal ensemble with nearly maximum entropy. To some extent, one could play with lattice geometry to induce the non-thermal behaviour. For example, in the case of the comb lattice structure, the model is non-integrable without any perturbation and the entropy growth of the scarred state is much slower than the thermalizing states for $J_a/J_e = 1.5$ (Fig. 4e, inset). In a two-dimensional-lattice SC device, the cross-couplings are still present and they lead to the scar state fully thermalizing by about 300–400 ns. Nevertheless, the thermalization timescale can be noticeably extended by periodic driving in the range of experimental capability (Supplementary Information).

Discussion and outlook

In summary, we have presented the first experimental realization of QMBS states in a solid-state SC platform. Our circuit emulates the effective hard-core Bose–Hubbard model—a model of particles freely hopping on both 1D and quasi-1D lattices, with local interactions. This is in contrast with previous realizations of QMBS in ultracold atomic systems[37,38], in which the particles' motion is kinetically constrained. Moreover, the underlying mechanism of scarring—approximate decoupling of a hypercube subgraph of the Hilbert space in the computational basis—is distinct from other platforms where QMBS is related to an underlying semiclassical periodic orbit[47]. Our study provides the first in-depth characterization of QMBS using quantum state tomography on large subsystems. By observing the population dynamics and entanglement entropy, we distinguished the weak ergodicity breaking associated with QMBS initial states from the conventional thermalizing states.

The realization of long-lived quantum states in strongly interacting solid-state systems has notable practical advantages compared with other mechanisms of ergodicity breaking, such as integrability and many-body localization. For example, although integrability is known to be fragile and limited to 1D systems, we demonstrated

that QMBS is robust to various imperfections such as random cross-couplings between qubits, and it persists beyond 1D systems. On the other hand, although strong ergodicity breaking in many-body localization systems may offer a more robust way of storing the initial-state information for longer times, for applications such as quantum-enhanced sensing and metrology[22], QMBS has the appealing property of extensive multipartite entanglement[48]. In this sense, it is important to note that the coupling strength of two qubits (associated with the oscillation frequency of a coherent many-body state, ~10^7 Hz) in our SC platform is extremely larger than other platforms such as a 1D Bose gas[49] (only around 10^3 Hz) and Rydberg atom[13] (~10^6 Hz), which means that the SC platform can process the same quantum information in a shorter time. These advantages of QMBS in an SC platform could be utilized for more practical quantum-sensing and metrology applications. On the fundamental side, our SC devices—with a rich palette of tomography-based probes—present a convenient setting to probe the interplay of scarred dynamics with localization on geometries with fractional dimensions and the emergence of diffusive transport in the conventional ETH limit.

Online content

Any methods, additional references, Nature Research reporting summaries, source data, extended data, supplementary information, acknowledgements, peer review information; details of author contributions and competing interests; and statements of data and code availability are available at https://doi.org/10.1038/s41567-022-01784-9.

References

1. Ladd, T. D. et al. Quantum computers. *Nature* **464**, 45–53 (2010).
2. Georgescu, I. M., Ashhab, S. & Nori, F. Quantum simulation. *Rev. Mod. Phys.* **86**, 153–185 (2014).
3. Mi, X. et al. Information scrambling in computationally complex quantum circuits. *Science* **374**, 1479–1483 (2021).
4. Arute, F. et al. Quantum supremacy using a programmable superconducting processor. *Nature* **574**, 505–510 (2019).
5. Swingle, B., Bentsen, G., Schleier-Smith, M. & Hayden, P. Measuring the scrambling of quantum information. *Phys. Rev. A* **94**, 040302 (2016).
6. Xu, K. et al. Emulating many-body localization with a superconducting quantum processor. *Phys. Rev. Lett.* **120**, 050507 (2018).
7. Landsman, K. A. et al. Verified quantum information scrambling. *Nature* **567**, 61–65 (2019).
8. Morong, W. et al. Observation of Stark many-body localization without disorder. *Nature* **599**, 393–398 (2021).
9. Deutsch, J. M. Quantum statistical mechanics in a closed system. *Phys. Rev. A* **43**, 2046–2049 (1991).
10. Srednicki, M. Chaos and quantum thermalization. *Phys. Rev. E* **50**, 888–901 (1994).
11. Rigol, M., Dunjko, V. & Olshanii, M. Thermalization and its mechanism for generic isolated quantum systems. *Nature* **452**, 854–858 (2008).
12. Kaufman, A. M. et al. Quantum thermalization through entanglement in an isolated many-body system. *Science* **353**, 794–800 (2016).
13. Bluvstein, D. et al. Controlling quantum many-body dynamics in driven Rydberg atom arrays. *Science* **371**, 1355–1359 (2021).
14. Serbyn, M., Abanin, D. A. & Papić, Z. Quantum many-body scars and weak breaking of ergodicity. *Nat. Phys.* **17**, 675–685 (2021).
15. Moudgalya, S., Bernevig, B. A. & Regnault, N. Quantum many-body scars and Hilbert space fragmentation: a review of exact results. *Rep. Prog. Phys.* **85**, 086501 (2022).
16. Heller, E. J. Bound-state eigenfunctions of classically chaotic Hamiltonian systems: scars of periodic orbits. *Phys. Rev. Lett.* **53**, 1515–1518 (1984).

17. Nandkishore, R. & Huse, D. A. Many-body localization and thermalization in quantum statistical mechanics. *Annu. Rev. Condens. Matter Phys.* **6**, 15–38 (2015).

18. Abanin, D. A., Altman, E., Bloch, I. & Serbyn, M. Colloquium: many-body localization, thermalization, and entanglement. *Rev. Mod. Phys.* **91**, 021001 (2019).

19. Guo, Q. et al. Stark many-body localization on a superconducting quantum processor. *Phys. Rev. Lett.* **127**, 240502 (2021).

20. Guo, Q. et al. Observation of energy-resolved many-body localization. *Nat. Phys.* **17**, 234–239 (2021).

21. Omran, A. et al. Generation and manipulation of Schrödinger cat states in Rydberg atom arrays. *Science* **365**, 570–574 (2019).

22. Dooley, S. Robust quantum sensing in strongly interacting systems with many-body scars. *PRX Quantum* **2**, 020330 (2021).

23. Shiraishi, N. & Mori, T. Systematic construction of counterexamples to the eigenstate thermalization hypothesis. *Phys. Rev. Lett.* **119**, 030601 (2017).

24. Moudgalya, S., Regnault, N. & Bernevig, B. A. Entanglement of exact excited states of Affleck-Kennedy-Lieb-Tasaki models: exact results, many-body scars, and violation of the strong eigenstate thermalization hypothesis. *Phys. Rev. B* **98**, 235156 (2018).

25. Schecter, M. & Iadecola, T. Weak ergodicity breaking and quantum many-body scars in spin-1 *XY* magnets. *Phys. Rev. Lett.* **123**, 147201 (2019).

26. Moudgalya, S., Bernevig, B. A. & Regnault, N. Quantum many-body scars in a Landau level on a thin torus. *Phys. Rev. B* **102**, 195150 (2020).

27. McClarty, P. A., Haque, M., Sen, A. & Richter, J. Disorder-free localization and many-body quantum scars from magnetic frustration. *Phys. Rev. B* **102**, 224303 (2020).

28. van Voorden, B., Minář, J. & Schoutens, K. Quantum many-body scars in transverse field Ising ladders and beyond. *Phys. Rev. B* **101**, 220305 (2020).

29. Hart, O., De Tomasi, G. & Castelnovo, C. From compact localized states to many-body scars in the random quantum comb. *Phys. Rev. Res.* **2**, 043267 (2020).

30. Zhao, H., Vovrosh, J., Mintert, F. & Knolle, J. Quantum many-body scars in optical lattices. *Phys. Rev. Lett.* **124**, 160604 (2020).

31. Kuno, Y., Mizoguchi, T. & Hatsugai, Y. Flat band quantum scar. *Phys. Rev. B* **102**, 241115 (2020).

32. O'Dea, N., Burnell, F., Chandran, A. & Khemani, V. From tunnels to towers: quantum scars from Lie algebras and *q*-deformed Lie algebras. *Phys. Rev. Res.* **2**, 043305 (2020).

33. Desaules, J.-Y., Hudomal, A., Turner, C. J. & Papić, Z. Proposal for realizing quantum scars in the tilted 1D Fermi-Hubbard model. *Phys. Rev. Lett.* **126**, 210601 (2021).

34. Ren, J., Liang, C. & Fang, C. Quasisymmetry groups and many-body scar dynamics. *Phys. Rev. Lett.* **126**, 120604 (2021).

35. Fendley, P., Sengupta, K. & Sachdev, S. Competing density-wave orders in a one-dimensional hard-boson model. *Phys. Rev. B* **69**, 075106 (2004).

36. Lesanovsky, I. & Katsura, H. Interacting Fibonacci anyons in a Rydberg gas. *Phys. Rev. A* **86**, 041601 (2012).

37. Bernien, H. et al. Probing many-body dynamics on a 51-atom quantum simulator. *Nature* **551**, 579–584 (2017).

38. Su, G.-X. et al. Observation of unconventional many-body scarring in a quantum simulator. Preprint at https://arxiv.org/abs/2201.00821 (2022).

39. Jepsen, P. N. et al. Long-lived phantom helix states in Heisenberg quantum magnets. *Nat. Phys.* **18**, 899–904 (2022).

40. Su, W. P., Schrieffer, J. R. & Heeger, A. J. Solitons in polyacetylene. *Phys. Rev. Lett.* **42**, 1698–1701 (1979).

41. Wu, Y. et al. Strong quantum computational advantage using a superconducting quantum processor. *Phys. Rev. Lett.* **127**, 180501 (2021).

42. Krantz, P. et al. A quantum engineer's guide to superconducting qubits. *Appl. Phys. Rev.* **6**, 021318 (2019).

43. Blais, A., Grimsmo, A. L., Girvin, S. M. & Wallraff, A. Circuit quantum electrodynamics. *Rev. Mod. Phys.* **93**, 025005 (2021).

44. Jafari, R. & Johannesson, H. Loschmidt echo revivals: critical and noncritical. *Phys. Rev. Lett.* **118**, 015701 (2017).

45. Najafi, K., Rajabpour, M. A. & Viti, J. Return amplitude after a quantum quench in the *XY* chain. *J. Stat. Mech.* **2019**, 083102 (2019).

46. Maimaiti, W., Andreanov, A., Park, H. C., Gendelman, O. & Flach, S. Compact localized states and flat-band generators in one dimension. *Phys. Rev. B* **95**, 115135 (2017).

47. Ho, W. W., Choi, S., Pichler, H. & Lukin, M. D. Periodic orbits, entanglement, and quantum many-body scars in constrained models: matrix product state approach. *Phys. Rev. Lett.* **122**, 040603 (2019).

48. Desaules, J.-Y., Pietracaprina, F., Papić, Z., Goold, J. & Pappalardi, S. Extensive multipartite entanglement from SU(2) quantum many-body scars. *Phys. Rev. Lett.* **129**, 020601 (2022).

49. Malvania, N. et al. Generalized hydrodynamics in strongly interacting 1D Bose gases. *Science* **373**, 1129–1133 (2021).

Methods

Device

We use an SC quantum processor in a flip-chip package, which hosts a square of 6×6 transmon qubits (Q_i) with 60 couplers (Q_c), each inserted between two neighbouring qubits (Fig. 1a). Each qubit (coupler) is a quantum two-level system with ground state $|0\rangle$ and excited state $|1\rangle$, whose energy separation can be dynamically tuned in the frequency range of 4.3–4.8 GHz (4.9–6.0 GHz). Each qubit has individual microwave (XY) and flux (Z) controls, and it is capacitively coupled to a readout resonator for state discrimination. Each coupler has an individual flux (Z) control and remains in the ground state during the experiment. We use high-precision synchronized analogue signals to control the qubits and couplers, with microwave pulses for qubit XY rotations and state readout, and square flux pulses for tuning the qubit and coupler frequencies. A complete experimental sequence consists of three stages: (1) state preparation where single-qubit π-pulses are applied to half the qubits, (2) multiqubit interaction stage where the nearest-neighbour qubit couplings are programmed by adjusting the couplers' frequencies and (3) the measurement stage where all the qubits are jointly read. We use two devices in main text, and the values of the relevant qubit parameters for device I such as the qubit operation frequencies, energy relaxation times (mean, ~50 μs) and single-qubit randomized benchmarking fidelities (mean, ~0.993) can be found in Supplementary Table 1 (also see the improved energy relaxation times for device II in Supplementary Table 2).

Effective model

We derive the effective spin-1/2 XY model for our experimental SC processor. The full Hamiltonian of the SC circuit system with both qubits and couplers is given by[42,50]

$$
\begin{aligned}
\mathcal{H}_{\text{full}}/\hbar = & \sum_i \left(\omega_i s_i^+ s_i^- + \frac{\eta_i}{2} s_i^+ s_i^+ s_i^- s_i^- \right) \\
& + \sum_c \left(\omega_c s_c^+ s_c^- + \frac{\eta_c}{2} s_c^+ s_c^+ s_c^- s_c^- \right) \\
& + \sum_{\langle i,j \rangle} g_{ij}(s_i^+ s_j^- + s_i^- s_j^+) \\
& + \sum_{\langle i,c \rangle} g_{ic}(s_i^+ s_c^- + s_i^- s_c^+),
\end{aligned}
\tag{1}
$$

where ω_i (ω_c) is the frequency of the ith qubit (coupler c), η_i (η_c) is the anharmonicity (or nonlinearity) of the ith qubit (coupler c), s_i^+ (s_i^-) is the creation (annihilation) operator of Q_i, g_{ij} (g_{ic}) is the coupling strength between Q_i and Q_j (Q_c) and the rotating-wave approximation is imposed on the qubit–coupler and qubit–qubit couplings. The subscripts (i, j) and c represent the indices of qubits and couplers, respectively. Also, $\langle i,j \rangle$ or $\langle i,c \rangle$ stands for the nearest-neighbour qubit–qubit or qubit–coupler pair, respectively. In these experiments, anharmonicity η_i is much larger than the couplings between the nearest-neighbour qubits (typically, $\eta_i/g_{ij} > 50$); therefore, the full Hamiltonian (1) can be reduced to the spin-1/2 XY Hamiltonian:

$$
\begin{aligned}
\mathcal{H}/\hbar = & \sum_i \omega_i s_i^+ s_i^- + \sum_c \omega_c s_c^+ s_c^- \\
& + \sum_{\langle i,j \rangle} g_{ij}(s_i^+ s_j^- + s_i^- s_j^+) + \sum_{\langle i,c \rangle} g_{ic}(s_i^+ s_c^- + s_i^- s_c^+).
\end{aligned}
\tag{2}
$$

We apply the Schrieffer–Wolff transformation $\mathcal{U} = e^{\mathcal{W}}$ to the Hamiltonian with

$$
\mathcal{W} = \sum_c \sum_i \frac{g_{ic}}{\Delta_{ic}}(s_i^+ s_c^- - s_i^- s_c^+),
$$

since all the qubits are far detuned from the couplers with $|\Delta_{ic}| = |\omega_i - \omega_c| \gg |g_{ic}|$. The effective Hamiltonian can then be approximated as

$$
\mathcal{H}_{\text{eff}}/\hbar \approx \sum_{\langle i,j \rangle} J_{ij}(s_i^+ s_j^- + s_i^- s_j^+) + \sum_i \Omega_i s_i^+ s_i^-,
\tag{3}
$$

where the effective coupling strength and transition frequencies are given by

$$
J_{ij} = g_{ij} + \sum_c g_{ic} g_{jc} \left[\frac{1}{\Delta_{ic}} + \frac{1}{\Delta_{jc}} \right],
\tag{4}
$$

$$
\Omega_i = \omega_i + \sum_c \frac{g_{ic}^2}{\Delta_{ic}},
\tag{5}
$$

respectively. The strength of indirect coupling can be tuned by adjusting the coupler frequency; therefore, the effective coupling strength $J_{ij}/2\pi$ can be dynamically tuned over a wide range, typically within $[-15, 1]$ MHz.

In our experiment, the chain and comb structures are formed by a snake-like qubit layout on a square lattice device; hence, the dominant cross-coupling cannot be neglected. The cross-perturbation Hamiltonian is given by

$$
\mathcal{H}_{\text{x}}/\hbar = \sum_{R_{ij} = \sqrt{2}a_0} J_{\text{x}}(i,j) \left[s_i^+ s_j^- + s_i^- s_j^+ \right],
\tag{6}
$$

where $R_{ij} = |\mathbf{r}_i - \mathbf{r}_j|$ is the separation distance of a qubit pair $\{i, j\}$. The couplings are in the range $J_{\text{x}}(i,j)/2\pi \in [0.3, 1.2]$ MHz and their measured values are given in the Supplementary Information. The magnitude of this perturbation is sufficiently large to break integrability of the model, as numerically demonstrated in the Supplementary Information.

Experimental sequence

Experimentally, we prepare a set of product states as the initial states and measure the final states of all the qubits as a function of the interaction time (the pulse sequence is shown in Extended Data Fig. 1). A typical experimental session starts by preparing the initial product state of all the qubits: each qubit Q_i is biased from its sweet spot to the corresponding idle frequency, where we apply single-qubit XY rotations. To prepare a high-fidelity state, during this period, the couplers are tuned such that the net couplings between the neighbouring qubits are turned off. To switch on the interactions among the qubits, we bias all the qubits to the interaction frequency and tune the coupler frequencies to turn on the couplings between the neighbouring qubits. After the interaction process, we bias all the qubits to their readout frequencies for measurements. All the directly measured qubit occupation probabilities are corrected to eliminate the measurement errors.

Numerics

We use the exact diagonalization method to numerically solve the eigenvalue problem and simulate the dynamics of the system. The basis of the Hamiltonian matrix is spanned by product states $|\alpha\rangle = |z_1\rangle \otimes |z_2\rangle \otimes |z_3\rangle \otimes \cdots \otimes |z_L\rangle$, also written as $|z_1 z_2 z_3 \cdots z_L\rangle$, where $z_j = 0$ or 1 represents the jth qubit at state $|0\rangle$ or $|1\rangle$, respectively. The elements of the Hamiltonian matrix are written as

$$
H_{\alpha\beta} = \langle \alpha | \mathcal{H} | \beta \rangle,
\tag{7}
$$

where α and β denote the index of the basis product states. Then, the eigenstate $|n\rangle$ and its eigenvalue E_n can be numerically solved from this Hamiltonian matrix. They are used to compute the spectrum-related quantities, such as entanglement entropy and overlap, as well as the dynamics of qubit populations, imbalance and wavefunction fidelity.

The Hamiltonian matrix is exponentially large in the number of qubits; to facilitate its diagonalization, we decompose it into smaller

sectors based on the symmetries of the model. For our spin-1/2 *XY* model with the open-boundary condition, these include particle conservation, reflection and symmetries. The original basis can be naturally divided into $L + 1$ uncoupled sectors, which conserve the particle number. The numerics throughout this paper are for the particle number equal to half the system size. Furthermore, to construct subspaces invariant under reflection and symmetries, we define a new set of basis states as

$$|\tilde{\alpha}(r,z)\rangle = \frac{1}{\sqrt{N_\alpha}} (1 + r\mathcal{R})(1 + z\mathcal{Z})|\alpha\rangle. \tag{8}$$

Here $r = \pm 1$ and $z = \pm 1$ are the eigenvalues of reflection- and inversion-symmetry generators $\mathcal{R}$ and $\mathcal{Z}$, respectively. Also, N_α is the normalization factor. The cross-couplings J_x break the reflection symmetry and the basis in this case is given by $|\tilde{\alpha}(z)\rangle = \left((1 + z\mathcal{Z})/\sqrt{N_\alpha}\right)|\alpha\rangle$.

We note that exact diagonalization is not the only numerical method available for this problem. However, alternative options are not well suited for studying QMBS in large systems. Methods based on Krylov subspace and matrix-product states could potentially access the dynamics from Π or Π' states for a few more qubits than 24. However, to show scarring requires studying the dynamics from a large number of initial states. In contrast to exact diagonalization, these two methods require an independent computation for each initial state. Furthermore, for MPS methods, it would also be costly to simulate the dynamics of thermalizing states as their entanglement entropy very quickly reaches the Page value. This would limit the simulation to a relatively short time, as the bond dimension of the matrix-product states (and consequently, the computational resources needed) required to faithfully capture the dynamics would rapidly become large.

Data availability
The data that support the findings of this study are available at https://doi.org/10.5518/1204.

Code availability
All the relevant source codes are available from the corresponding authors upon reasonable request.

References
50. Neill, C. et al. A blueprint for demonstrating quantum supremacy with superconducting qubits. *Science* **360**, 195–199 (2018).

Author contributions
L.Y. proposed the idea. L.Y., Y.-C.L., J.Y.D. and Z.P. developed the theory and numerical simulation. P.Z., H.D. and Y.G. performed the experiment, and H.L. and J.C. fabricated the device supervised by H.W. L.Z. and J.H. developed the measurement electronics. L.Y., H.W., Y.-C.L. and Z.P. co-wrote the manuscript. All the authors contributed to the experimental setup, discussions of the results and development of the manuscript.

Competing interests
The authors declare no competing interests.

Additional information
**Extended data** is available for this paper at https://doi.org/10.1038/s41567-022-01784-9.

Supplementary information The online version contains supplementary material available at https://doi.org/10.1038/s41567-022-01784-9.

Correspondence and requests for materials should be addressed to Lei Ying, H. Wang or Ying-Cheng Lai.

Peer review information *Nature Physics* thanks the anonymous reviewers for their contribution to the peer review of this work

Reprints and permissions information is available at www.nature.com/reprints.
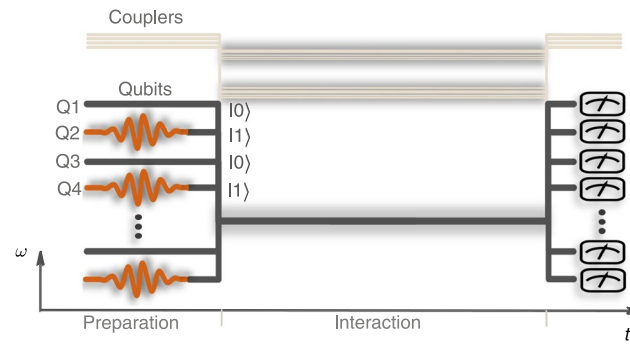
Extended Data Fig. 1 | Experimental sequence diagram. Sequence with strongly interacting many-body dynamics, where injecting a π pulse (red wave pulse) serves to lift the two-level qubit from the ground state to the excited state.